Contents lists available at ScienceDirect

Earth and Planetary Science Letters

A viscoplastic shear-zone model for deep (15–50 km) slow-slip events at plate convergent margins

An Yin [*], Zhoumin Xie, Lingsen Meng

Department of Earth, Planetary, and Space Sciences, University of California, Los Angeles, CA 90095-156702, USA

A B S T R A C T

A key issue in understanding the physics of deep (15–50 km) slow-slip events (D-SSE) at plate convergent margins is how their initially unstable motion becomes stabilized. Here we address this issue by quantifying a rate-strengthening mechanism using a viscoplastic shear-zone model inspired by recent advances in field observations and laboratory experiments. The well-established segmentation of slip modes in the downdip direction of a subduction shear zone allows discretization of an interseismic forearc system into the (1) frontal segment bounded by an interseismically locked megathrust, (2) middle segment bounded by episodically locked and unlocked viscoplastic shear zone, and (3) interior segment that slips freely. The three segments are assumed to be linked laterally by two springs that tighten with time, and the increasing elastic stress due to spring tightening eventually leads to plastic failure and initial viscous shear. This simplification leads to seven key model parameters that dictate a wide range of mechanical behaviors of an idealized convergent margin. Specifically, the viscoplastic rheology requires the initially unstable sliding to be terminated nearly instantaneously at a *characteristic velocity*, which is followed by stable sliding (i.e., slow-slip). The characteristic velocity, which is on the order of $<10^{-7}$ m/s for the convergent margins examined in this study, depends on the (1) effective coefficient of friction, (2) thickness, (3) depth, and (4) viscosity of the viscoplastic shear zone. As viscosity decreases exponentially with temperature, our model predicts faster slow-slip rates, shorter slow-slip durations, more frequent slow-slip occurrences, and larger slow-slip magnitudes at warmer convergent margins.

© 2018 Elsevier B.V. All rights reserved.

1. Introduction

Deep (15–50 km) slow-slip events (D-SSEs) occur along the upper interface of a subducting slab (Shelly et al., 2006; Ide et al., 2007a) at the brittle–ductile transition (BDT) depths (Peacock et al., 2011) between the up-dip seismogenic megathrust and the down-dip aseismic creeping zone (Schwartz and Rokosky, 2007; cf., Gao and Wang, 2017) (Figs. 1a and 1b). Individual events accommodate a few cm motion, rupture up to >1000 s km^2, last a few days to a few years (e.g., Dragert et al., 2001; Szeliga et al., 2008), are accompanied by tectonic tremors and/or microseismicity (Dragert et al., 2001; Obara and Kato, 2016; Gao and Wang, 2017), and have maximum stress drops of 10–100 kPa (Ide et al., 2007b; Brodsky and Mori, 2007). When the continental interior above a subducting slab is fixed, slow-slip motion in a forearc region may be expressed in two contrasting modes: (1) alternating fast and slow episodes of landward motion with the slow-slip phase mov-

ing at a rate slower than the speed of the subducting slab (i.e., $V_{HW} < V_{FW}$ and V_{HW} and $V_{FW} > 0$) (Fig. 1c), or (2) alternating landward and trenchward motion with the hanging wall moving in the opposite direction of the subducting footwall motion (i.e., $V_{HW} < 0$ and $V_{FW} > 0$) (Fig. 1d). As shown in Figs. 1c and 1d, V_{HW} is the hanging-wall/overriding-plate velocity, and V_{FW} is the footwall/subducting-plate velocity; they are positive in the landward direction. Note that the slow-slip mode via alternating fast and slow landward motion has not been documented formally, although the geodetic observations do hint their existence despite the large noise-signal ratios (e.g., Dragert et al., 2001).

Most D-SSEs are quasi-periodic (e.g., Szeliga et al., 2008), interpreted as a result of conditionally stable sliding governed by rate-state friction such as the work of Liu and Rice (2007) and Liu (2013) based on a gabbro rate-state friction law (He et al., 2007). As subduction shear zones are composed of felsic and mafic rocks with drastically different rheological properties (e.g., Grove et al., 2008; Hayman and Lavier, 2014), the composite effects of mixed rock rheology must be considered. In this regard, He et al. (2013) demonstrated experimentally that the presence of a trace amount of quartz in gabbro gouge under the deep slow-slip condi-
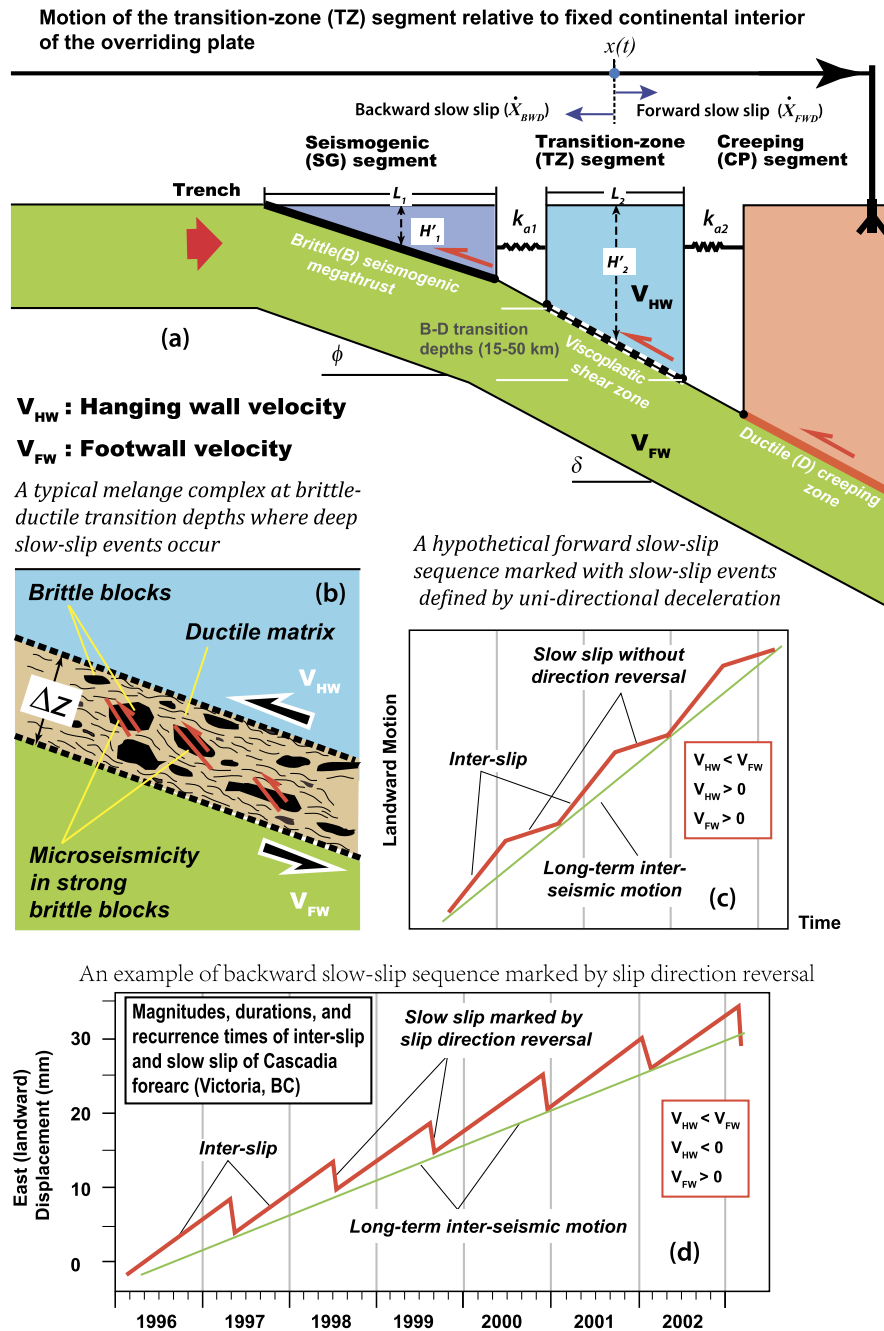
Fig. 1. (a) Forearc division of an overriding plate at a convergent margin: SG, seismogenic segment bounded below by a brittle seismogenic fault; TZ, brittle–ductile transition-zone segment bounded below by a viscoplastic shear zone along which deep slow-slip events occur; CP, creeping segment bounded by an aseismic ductile shear zone. (b) A conceptualized deep slow-slip shear zone that consists of strong and partially interlocked brittle blocks (mafic rocks and/or strong mineral phases cut by brittle faults and fractures) surrounded by ductile matrix (felsic and phyllosilicate rocks with mylonitic fabrics). (c) A hypothetical mode of a slow-slip sequence expressed by alternating fast and slow landward motion. (d) A slow-slip sequence characterized by alternating landward and trenchward motion as recorded in the Cascadia forearc, simplified after Rogers and Dragert (2003).

tions would lead to stable frictional sliding, which puts the results of Liu and Rice (2007) and Liu (2013) in question.

Assuming the onset of a slow-slip event is unstable due to rate-weakening governed by rate-state friction, dilatancy (e.g., Segall et al., 2010) and high-velocity strengthening (e.g., Shimanmoto and Noda, 2014) were proposed as possible stabilization mechanisms during slow-slip events. For dilatancy to work, particles in the shear zone must be rigid, in frictional contact, and closely compacted (Reynolds, 1885). However, the clast-supported texture required by the dilatancy mechanism contrasts the characteristic *ductile* matrix-supported texture of exhumed subduction

shear zones from the D-SSE depths (e.g., Grove et al., 2008; Hayman and Lavier, 2014; Angiboust et al., 2015) (Fig. 1b). The high-velocity strengthening mechanism is also problematic, as it has never been confirmed experimentally with the lithology and pressure–temperature conditions relevant to D-SSEs (e.g., He et al., 2013).

Temperature as a state variable, neglected in the existing modeling efforts (e.g., Liu and Rice, 2007), plays a dominant role in frictional sliding under the brittle–ductile transition temperatures (400–600°C) (Chester, 1994). Additionally, shear-zone thickness, which is also not treated in the existing slow-slip models (e.g.,

Segall et al., 2010), also dictates the rheological behaviors of rock deformation under the brittle–ductile transition conditions (e.g., Pec et al., 2016). Comparison of rock fabrics in exhumed subduction shear zones against experimentally determined microstructures indicates viscoplasticity dominates deformation under the D-SSE conditions (e.g., Zhang and He, 2016; Pec et al., 2016). Indeed, analogue (Reber et al., 2015) and thermomechanical modeling (Gao and Wang, 2017) all require viscoplasticity at the brittle–ductile transition depths to explain D-SSE-related observations.

Departing from the rate-state friction laws, a fault with arbitrarily assigned clusters of viscoplastic and ductile patches was used to simulate D-SSEs (e.g., Nakata et al., 2011). As the fault in their model has no thickness, a fictitious viscosity factor has to be assumed, which cannot be related to any real rock properties. Lavier et al. (2013) was able to simulate cyclic slip events along the interface of two viscous layers under horizontal shear (also see Hayman and Lavier, 2014). However, the simple model geometry and omission of plasticity make the model unsuitable as a general D-SSE mechanism. Serpentine dehydration (e.g., Poulet et al., 2014) was modeled in the context of viscoplastic deformation along a subduction zone, but the omission of silica precipitation and dissolution, possibly a dominant process along deep slow-slip shear zones (Audet and Bürgmann, 2014), casts doubts on the applicability of this mechanism for D-SSEs.

To our knowledge, no viscoplastic models have attempted to relate durations, magnitudes, and recurrence times of D-SSEs to the plastic strength, effective viscosity, and thickness of the corresponding shear zone at convergent margins. To address this issue, we perform a set of simple mechanical analyses on a discretized interseismic forearc system consisting of the seismogenic (SG), transition-zone (TZ), and creeping-zone (CP) segments linked by elastic springs and bounded below by the seismogenic (SG), viscoplastic slow-slip (TZ), and aseismic creeping (CP) shear zones, respectively (Fig. 1a). The above division is based on the well-established down-dip segmentation of slip modes across forearc regions where D-SSEs were recorded (e.g., Schwartz and Rokosky, 2007; Obara and Kato, 2016). Although long-term and short-term deep slow-slip events are separated spatially at some convergent margins (Gao and Wang, 2017), this study lumps the two domains together as a single shear zone directly below the transition-zone (TZ) block. Temporally, we evaluate force balance of the transition-zone (TZ) segment during a full slow-slip cycle, which consists of (1) an *inter-slip* phase (denoted as IS) when the shear zone below is locked, and (2) a *slow-slip* phase (denoted as SS) when the shear zone below is unlocked. Shallow slow-slip events (S-SSEs) near the trench (e.g., Wallace et al., 2016; Araki et al., 2017) are not treated here. For simplicity, we assume that a seismogenic fault reaches all the way to the surface at the trench (Fig. 1a). We are aware of the cases such as the NE Japan subduction zone where slow-slip and seismogenic zones were postulated to overlap along the upper interface of the subducting slab (Kato et al., 2012; Ito et al., 2013). However, it is unclear whether this inference is an artefact of poor spatial resolutions that are unable to differentiate the inter-slab seismicity from the slab-interface seismicity.

The aim of this paper is to (1) provide a quenching mechanism for stabilizing a slow-slip event, and (2) place bounds on the rheological properties of deep slow-slip shear zones at convergent margins using the magnitudes, durations, and recurrence times of cyclic slow-slip events. The major results of this work are the quantification of several key dimensionless parameters that govern the end-member mechanical behaviors of convergent margins with or without the association of D-SSEs. Simulating fully cyclic slip sequences is beyond the scope of this study.

2. Model setup

2.1. Evolution of a cyclic slow-slip sequence

Motion of a forearc region towards the fixed continental interior is regarded in this study as "forward" or "landward" in the positive x-axis direction, whereas motion away from the fixed continental interior is referred to as "backward" or "trenchward" in the negative x-axis direction (Fig. 1a). This definition is independent of whether the slow-slip shear zone below is locked during the inter-slip phase or unlocked during the slow-slip phase. Accordingly, a megathrust event is associated with backward/trenchward motion in the negative direction of the x-axis (Fig. 1a).

A cyclic slow-slip sequence starts with a cycle number $i = 1$ immediately after a megathrust event and ends with a cycle number $i = i_{max}$ immediately before the next megathrust event (Fig. 2). We use two time-dependent displacement variables x and X and two corresponding time sequences t and t' to track the motion of the transition-zone (TZ) segment:

(i) $x(t)$ for the total displacement starting at $t = 0$, and
(ii) $X_{(i)}(t')$ for the incremental slip in the i-th slip cycle starting at $t' = t - t_i = 0$, where t_i is the starting time of the i-th cycle.

Here, the subscript i is the slip cycle number. At the end of the i-th slip cycle, the incremental shortenings of springs 1 and 2 are referred to as $\Delta x^{(1)}$ and $\Delta x^{(2)}$, where the superscripts (1) and (2) indicate the spring number as shown in Fig. 1; spring 1 links the SG and TZ blocks and spring 2 links the TZ and CP blocks. As we assume the motion in a cyclic slow-slip sequence is repetitive, the total shortenings in the two springs since $t = 0$ at the end of the i-th cycle are $i\Delta x^{(1)}$ and $i\Delta x^{(2)}$, respectively (Table 1).

We consider each slow-slip cycle to consist of an inter-slip phase and a slow-slip phase as illustrated in Fig. 2. Below we describe the evolution of a full slow-slip cycle in a simple conceptual model along a horizontal slip surface. In our actual model, the gravitational effect on an inclined subduction zone is considered.

(1) *The onset of a cyclic slip sequence* starts after a coseismic megathrust event that ruptures both the seismogenic fault and the slow-slip shear zone either during the main seismic phase or through afterslip deformation (Fig. 2a) (e.g., Hu et al., 2016; Gao and Wang, 2017). At this time springs 1 and 2 may still preserve relic strains, represented by remaining shortening as $x_0^{(1)}$ and $x_0^{(2)}$. Displacements of the seismogenic (SG) and transition-zone segments (TZ), denoted as $x_{SG}(t)$ and $x_{TZ}(t)$, are related to the spring shortenings $x^{(1)}(t)$ and $x^{(2)}(t)$ by

$$x_{SG}(t) = x^{(1)}(t) - x_0^{(1)},$$
$$x_{TZ}(t) = x^{(2)}(t) - x_0^{(2)}.$$

(2) An *inter-slip phase* occurs when the viscoplastic slow-slip shear zone is locked and the seismogenic (SG) and transition-zone (TZ) blocks move at the same speed as the footwall speed (i.e., $V_{HW} = V_{FW}$). The total inter-slip motion $S_{TZ(i)}^{IS}$ for the transition-zone (TZ) block is $S_{TZ(i)}^{IS} = V_{FW}\Delta T_{TZ(i)}^{IS}$, where $\Delta T_{TZ(i)}^{IS}$ is the inter-slip phase duration in the i-th slow-slip cycle (Figs. 2b and 2c). Here superscript IS refers to the inter-slip phase, and quantities $S_{TZ(i)}^{IS}$, V_{FW}, and $\Delta T_{TZ(i)}^{IS}$ are observables.

(3) Following Segall et al. (2010), we assume the onset of a slow-slip event *unstable* due to initial rate-weakening of the shear zone (Fig. 2d). In our model, we treat the unstable sliding episode as a transient event that is replaced instantaneously by *stable sliding* at the onset of a slow-slip phase (Fig. 2e). As such, the total
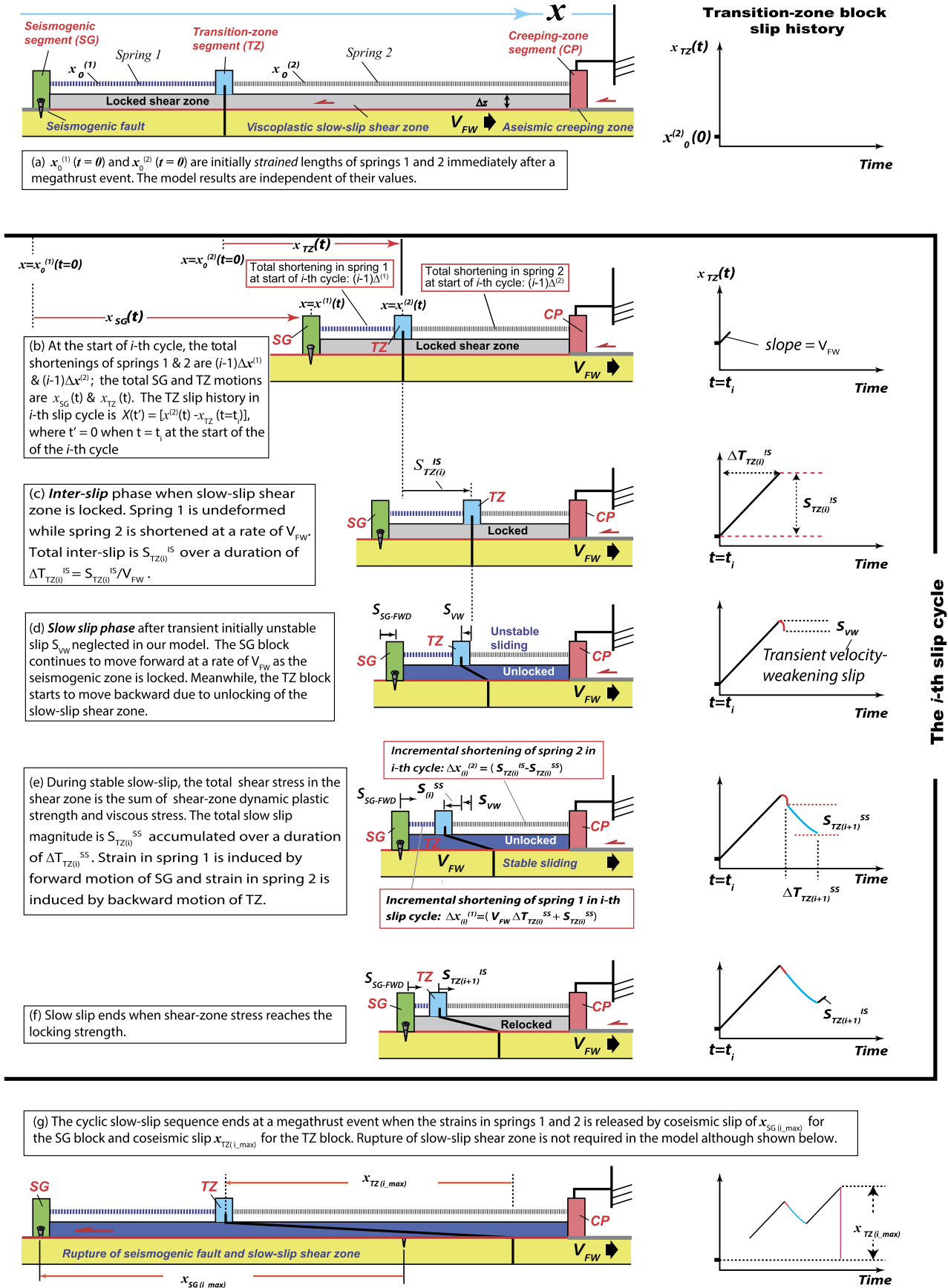
Transition-zone block slip history

$x_{TZ}(t)$

$x^{(2)}_{0}(0)$

Time

Seismogenic segment (SG)

Spring 1

$x_0^{(1)}$

Transition-zone segment (TZ)

$x_0^{(2)}$

Spring 2

Creeping-zone segment (CP)

Δz

Locked shear zone

Seismogenic fault

Viscoplastic slow-slip shear zone

V_{FW}

Aseismic creeping zone

(a) $x_0^{(1)}(t=0)$ and $x_0^{(2)}(t=0)$ are initially *strained* lengths of springs 1 and 2 immediately after a megathrust event. The model results are independent of their values.

$x = x_0^{(1)}(t=0)$

$x = x_0^{(2)}(t=0)$

$x_{TZ}(t)$

Total shortening in spring 1 at start of *i*-th cycle: $(i-1)\Delta^{(1)}$

Total shortening in spring 2 at start of *i*-th cycle: $(i-1)\Delta^{(2)}$

$x_{SG}(t)$

$x = x^{(1)}(t)$

$x = x_i^{(2)}(t)$

CP

SG

TZ

Locked shear zone

V_{FW}

(b) At the start of *i*-th cycle, the total shortenings of springs 1 & 2 are $(i-1)\Delta x^{(1)}$ & $(i-1)\Delta x^{(2)}$; the total SG and TZ motions are $x_{SG}(t)$ & $x_{TZ}(t)$. The TZ slip history in *i*-th slip cycle is $X(t') = [x^{(2)}(t) - x_{TZ}(t=t_i)]$, where $t' = 0$ when $t = t_i$ at the start of the of the *i*-th cycle

$x_{TZ}(t)$

$slope = V_{FW}$

$t = t_i$

Time

(c) *Inter-slip* phase when slow-slip shear zone is locked. Spring 1 is undeformed while spring 2 is shortened at a rate of V_{FW}. Total inter-slip is $S_{TZ(i)}^{IS}$ over a duration of $\Delta T_{TZ(i)}^{IS} = S_{TZ(i)}^{IS}/V_{FW}$.

$S_{TZ(i)}^{IS}$

SG

TZ

CP

Locked

V_{FW}

$\Delta T_{TZ(i)}^{IS}$

$S_{TZ(i)}^{IS}$

$t = t_i$

Time

(d) *Slow slip phase* after transient initially unstable slip S_{VW} neglected in our model. The SG block continues to move forward at a rate of V_{FW} as the seismogenic zone is locked. Meanwhile, the TZ block starts to move backward due to unlocking of the slow-slip shear zone.

S_{SG-FWD}

S_{VW}

Unstable sliding

SG

TZ

CP

Unlocked

V_{FW}

S_{VW}

Transient velocity-weakening slip

$t = t_i$

Time

(e) During stable slow-slip, the total shear stress in the shear zone is the sum of shear-zone dynamic plastic strength and viscous stress. The total slow slip magnitude is $S_{TZ(i)}^{SS}$ accumulated over a duration of $\Delta T_{TZ(i)}^{SS}$. Strain in spring 1 is induced by forward motion of SG and strain in spring 2 is induced by backward motion of TZ.

Incremental shortening of spring 2 in i-th cycle: $\Delta x_{(i)}^{(2)} = (S_{TZ(i)}^{IS} - S_{TZ(i)}^{SS})$

S_{SG-FWD}

$S_{(i)}^{SS}$

S_{VW}

SG

TZ

CP

Unlocked

V_{FW}

Stable sliding

Incremental shortening of spring 1 in i-th slip cycle: $\Delta x_{(i)}^{(1)} = (V_{FW}\Delta T_{TZ(i)}^{SS} + S_{TZ(i)}^{SS})$

$S_{TZ(i+1)}^{SS}$

$t = t_i$

Time

$\Delta T_{TZ(i+1)}^{SS}$

(f) Slow slip ends when shear-zone stress reaches the locking strength.

S_{SG-FWD}

TZ

$S_{TZ(i+1)}^{IS}$

SG

CP

Relocked

V_{FW}

$S_{TZ(i+1)}^{IS}$

$t = t_i$

Time

The *i*-th slip cycle

(g) The cyclic slow-slip sequence ends at a megathrust event when the strains in springs 1 and 2 is released by coseismic slip of $x_{SG(i\_max)}$ for the SG block and coseismic slip $x_{TZ(i\_max)}$ for the TZ block. Rupture of slow-slip shear zone is not required in the model although shown below.

SG

TZ

$x_{TZ(i\_max)}$

CP

Rupture of seismogenic fault and slow-slip shear zone

V_{FW}

$x_{SG(i\_max)}$

$x_{TZ(i\_max)}$

Time

Fig. 2. A conceptual model for the kinematic and mechanical evolution of a slow-slip cycle along a flat shear zone. A cyclic slow-slip sequence occurs between two megathrust events as shown in (a) and (g), which rupture the seismogenic and slow-slip shear zones. (b) to (f) illustrate how a single slow-slip cycle, which consists of an inter-slip phase and a slow-slip phase, evolves with time. See text for explanation and Table 1 for the definition of the key model parameters.

Table 1
List of model parameters and constants.

---

1. Input parameters and constants in viscoplastic solution

$\overline{\mu}_{s(i)}^{TZ} = (1 - \lambda_{s(i)}^{TZ})\mu_{s(i)}^{TZ}$, effective static friction with $\lambda_{s(i)}^{TZ}$ and $\mu_{s(i)}^{TZ}$ as pore-pressure ratio and friction coefficient.

$\overline{\mu}_{d(i)}^{TZ} = (1 - \lambda_{d(i)}^{TZ})\mu_{d(i)}^{TZ}$, effective dynamic friction with $\lambda_{d(i)}^{TZ}$ and $\mu_{d(i)}^{TZ}$ as pore-pressure ratio and friction coefficient.

$\overline{\mu}_{L(i)}^{TZ} = (1 - \lambda_{L(i)}^{TZ})\mu_{L(i)}^{TZ}$, effective locking friction with $\lambda_{L(i)}^{TZ}$ and $\mu_{L(i)}^{TZ}$ as pore-pressure ratio and friction coefficient.

$\Delta\overline{\mu}_{(s-d)(i)}^{TZ} \equiv (\overline{\mu}_{s(i)}^{TZ} - \overline{\mu}_{d(i)}^{TZ}) \approx \frac{\Delta\sigma_{drop(i)\_max}}{\rho g H_2' \cos(\delta)}$, Differential friction coefficient.

$Y_{s(i)}^{TZ} \equiv \overline{\mu}_{s(i)}^{TZ} \rho g H_2' \cos(\delta)$, $Y_{d(i)}^{TZ} \equiv \overline{\mu}_{d(i)}^{TZ} \rho g H_2' \cos(\delta)$, $Y_{L(i)}^{TZ} \equiv \overline{\mu}_{L(i)}^{TZ} \rho g H_2' \cos(\delta)$: static/dynamic/locking strength.

$F_{f(i)}^{TZ} = \overline{\mu}_{s(i)}^{TZ} \rho g H_2' L_2 W(t)$, frictional force, with L_2 and $W(t)$ as length and width of the slow-slip shear zone.

$F_{e(i)}^{TZ/IS} = [x_0^{(1)} + i\Delta x_{(i)}^{(1)}]k_{a1} - [x_0^{(2)} + i\Delta x_{(i)}^{(2)} + V_{FW}\Delta T_{IS(i)}]k_{2a}$, elastic force during inter-slip.

$F_{e(i)}^{TZ/SS} = [x_0^{(1)} + i\Delta x_{(i)}^{(1)}]k_{a1} - [x_0^{(2)} + i\Delta x_{(i)}^{(2)}]k_{a2}$, elastic force during slow slip.

$F_{vp(i)}^{TZ} = \frac{\{\Delta z \cos(\delta)\overline{\mu}_{d(i)}^{TZ}\rho g H_2' + \eta_e[V_{FW} \pm |\dot{X}(t')|]\cos(\delta)\}W(t)L_2}{\Delta z \cos(\delta)}$, viscoplastic force during slow slip.

$F_g^{TZ} = \rho g \sin(\delta) H_2' L_2 W(t)$, gravitational forces on TZ block.

$b = \frac{\eta}{\Delta z \rho H_2' \cos(\delta)}$, $c = (\frac{H_1'}{L_1}E_1 + \frac{H_2'}{L_2}E_2)\frac{1}{\rho H_2' L_2}$, $d_{0(i)}^{FWD/BWD} = \pm\frac{(\overline{\mu}_d - \overline{\mu}_s)\Delta z \rho H_2' g + \eta_e V_{FW}}{\Delta z \rho H_2' \cos(\delta)}$, $d_1^{FWD/BWD} = \pm\frac{V_{FW}E_1 H_1'}{\rho H_2' L_1 L_2}$.

$C_{1(i)}^{FWD} = \frac{-2cV_{cr(i)}^{FWD} + 2d_1^{FWD} - (d_{0(i)}^{FWD} - \frac{bd_1^{FWD}}{c})(\sqrt{b^2-4c}-b)}{2c(\sqrt{b^2-4c})}$, $C_{2(i)}^{FWD} = \frac{2cV_{cr(i)}^{FWD} - 2d_1^{FWD} - (d_{0(i)}^{FWD} - \frac{bd_1^{FWD}}{c})(\sqrt{b^2-4c}+b)}{2c(\sqrt{b^2-4c})}$.

$C_{1(i)}^{BWD} = \frac{-2cV_{cr(i)}^{BWD} + 2d_1^{BWD} - (d_{0(i)}^{BWD} - \frac{bd_1^{BWD}}{c})(\sqrt{b^2-4c}-b)}{2c(\sqrt{b^2-4c})}$, $C_{2(i)}^{BWD} = \frac{2cV_{cr(i)}^{BWD} - 2d_1^{BWD} - (d_{0(i)}^{BWD} - \frac{bd_1^{BWD}}{c})(\sqrt{b^2-4c}+b)}{2c(\sqrt{b^2-4c})}$.

2. Model-derived parameters

(1) *Strain partitioning coefficient* $\alpha_i = \frac{\Delta x^{(2)}}{\Delta x_i^{(1)}}$: forearc front overshooting when $\alpha_i < 1$ and undershooting when $\alpha_i > 1$.

(2) *Critical strain partitioning coefficient* $\alpha_{cr} = \frac{H_1' L_2}{H_2' L_1}\frac{E_1}{E_2}$: strengthen hardening or weakening when $\alpha_i > \alpha_{cr}$ or $\alpha_i < \alpha_{cr}$.

(3) *Characteristic viscosity* $\eta^* = \frac{\Delta z(\Delta\overline{\mu}_{(s-d)(i)}^{TZ})\rho g H_2'}{\cos(\delta)V_{FW}}$: forward slow slip when $\eta_e < \eta^*$ and backward slow slip when $\eta_e > \eta^*$.

(4) *Critical viscosity* $\eta_{cr} = 2\Delta z \rho H_2' \cos(\delta)\sqrt{(\frac{H_1'}{L_1}E_1 + \frac{H_2'}{L_2}E_2)\frac{1}{\rho H_2' L_2}}$: oscillation motion when $\eta_e < \eta_{cr}$, exponential decay motion when $\eta_e > \eta_{cr}$.

(5) *Characteristic velocity* $V_{cr(i)} = \pm\frac{\Delta\overline{\mu}_{(s-d)(i)}^{TZ}\rho g H_2' \Delta z - \eta_e V_{FW}}{\cos(\delta)\eta_e}$: slow slip starts when hanging-wall velocity $\geq V_{cr(i)}$.

(6) *Locking velocity* $V_{L(i)} = \pm\frac{(\overline{\mu}_{L(i)}^{TZ} - \overline{\mu}_{d(i)}^{TZ})\rho g H_2' \Delta z - \eta_e V_{FW}}{\eta_e}$: slow slip terminates when hanging-wall velocity reaches $V_{L(i)}$.

(7) *Incremental strength change* $\Delta\overline{\mu}_{s(i)}^{TZ} = \frac{\Delta x_{(i)}^{(2)}\cos(\delta)(\frac{H_2'}{L_2}E_2 - \frac{H_1'}{\alpha_i L_1}E_1)}{\rho g H_2' L_2}$: shear zone strengthening $(\Delta\overline{\mu}_{s(i)}^{TZ} > 0)$/weakening $(\Delta\overline{\mu}_{s(i)}^{TZ} < 0)$ from slip cycle $(i-1)$ to slip cycle (i).

---

displacement of the transition-zone (TZ) block at the start of the i-th slow-slip cycle is

$$x_{TZ}(t) = x_{TZ(i)} \quad (t = t_i),$$

and its incremental slow-slip history since $t' = t - t_i = 0$ is

$$X_{TZ(i)}(t') = x_{TZ}(t) - x_{TZ(i)} \quad (t = t_i).$$

Again, $t' = t - t_i = 0$ represents the starting time of the i-th slow-slip cycle. We denote $S_{TZ(i)}^{SS}$ and $\Delta T_{TZ(i)}^{SS}$ as the total incremental slow-slip magnitude and duration at the end of the i-th slip cycle, where superscript SS refers to the slow-slip phase. In our notation, $X(t')$ is a time-dependent variable, whereas $S_{TZ(i)}^{SS}$ is an observable and a constant. The two quantities are related by $X_{TZ(i)}(t' = \Delta T_{TZ(i)}^{SS}) = S_{TZ(i)}^{SS}$.

(4) At the end of each slow-slip cycle, the total incremental shortenings in springs 1 and 2 are:

$$\Delta x^{(1)} = \Delta x_{(i)}^{(1)} = (V_{FW}\Delta T_{TZ(i)}^{SS} + S_{TZ(i)}^{SS}),$$

$$\Delta x^{(2)} = \Delta x_{(i)}^{(2)} = (S_{TZ(i)}^{IS} - S_{TZ(i)}^{SS}),$$

and their ratio, referred here as *strain-partitioning coefficient*, is

$$\alpha_i = \frac{\Delta x_{(i)}^{(2)}}{\Delta x_{(i)}^{(1)}} = \frac{\Delta x^{(2)}}{\Delta x^{(1)}},$$

where $\alpha_i < 1$ indicates more elastic strain is stored in spring 1 near the trench and $\alpha_i > 1$ indicates more elastic strain is stored in spring 2 away from the trench.

(5) A slow-slip event terminates when the shear-zone stress reaches its locking strength (Fig. 2f), while a cyclic slow-slip sequence ends with a megathrust event accompanied by coseismic slip of the SG and TZ blocks denoted as $x_{SG(i_{\max})}$ and $x_{TZ(i_{\max})}$ in Fig. 2g and are related to the shortenings of the two springs and slip cycle numbers by

$$x_{SG(i_{\max})} = i_{\max}\Delta x^{(1)},$$

$$x_{SG(i_{\max})} = i_{\max}\Delta x^{(2)},$$

$$x_{SG(i_{\max})} = \frac{1}{\alpha_i}x_{TZ(i_{\max})}.$$

Note that $x_{SG(i_{\max})} > x_{SG(i_{\max})}$ (i.e., $\alpha_i < 1$) requires a larger coseismic slip near the trench, which may represent the well-known overshooting situations during a megathrust event typically expressed by coeval forearc extension (e.g., Ide et al., 2011; Huang et al., 2014). In contrast, $x_{SG(i_{\max})} < x_{SG(i_{\max})}$ (i.e., $\alpha_i < 1$) requires a less coseismic slip near the trench, which may represent a undershooting situation during a megathrust event (Huang et al., 2014).

2.2. Mechanical properties and force balances at a convergent margin

Although we treat the seismogenic (SG) and transition-zone (TZ) segments as rigid blocks in the model (Fig. 2), their elastic properties are not ignored but assigned to the linking springs through the axial stiffness:

$$k_{a1} = \frac{W(t)H_1'}{L_1}E_1 \quad \text{for the seismogenic (SG) block}$$

$$k_{a2} = \frac{W(t)H_2'}{L_2}E_2 \quad \text{for the transition-zone (TZ) block}$$

where $W(t)$ is the width of the seismogenic and slow-slip rupture zones that expands with time during thrust/shear-zone rupturing; H'_1 and H'_2 are averaged thickness of the seismogenic and transition-zone blocks; L_1 and L_2 are horizontal lengths; and E_1 and E_2 are Young's modulus of the seismogenic (SG) and transition-zone (TZ) blocks (Fig. 1a). It is important to note that the *axial* stiffness differs from the *rotational* stiffness $k_r = \frac{J}{L}G$ in frictional instability analyses (e.g., Segall et al., 2010), where J is torsion constant, G is shear rigidity, and L is slip-plane length (pp. 1–11, Wilson, 2002).

The mechanical properties of the slow-slip shear zone are the *effective* coefficients of static ($\overline{\mu}_{s(i)}^{TZ}$ in Table 1), dynamic ($\overline{\mu}_{d(i)}^{TZ}$ in Table 1), and locking ($\overline{\mu}_{L(i)}^{TZ}$ in Table 1) friction, and the effective viscosity (η_e). Here, superscript TZ denotes the slow-slip shear zone below the transition-zone (TZ) block. The three friction coefficients are related to three plastic yield strengths of the slow-slip shear zone at three different stages of a slow-slip cycle (Table 1):

$$Y_{s(i)}^{TZ} \equiv \overline{\mu}_{s(i)}^{TZ} \rho g H'_2 \cos(\delta)$$
$$Y_{d(i)}^{TZ} \equiv \overline{\mu}_{d(i)}^{TZ} \rho g H'_2 \cos(\delta)$$
$$Y_{L(i)}^{TZ} \equiv \overline{\mu}_{L(i)}^{TZ} \rho g H'_2 \cos(\delta)$$

where δ is the dip angle of the shear zone, ρ hanging wall density, and g gravitational acceleration. Note that $\overline{\mu}_{s(i)}^{TZ}$, $\overline{\mu}_{d(i)}^{TZ}$, and $\overline{\mu}_{L(i)}^{TZ}$ *are not material constants* but could vary with time due to changes in pore-fluid-pressure ratios (Table 1) and/or fault healing (e.g., Yasuhara et al., 2005; Xue et al., 2013) in a slow-slip cycle. In general, $Y_{s(i)}^{TZ} \neq Y_{L(i)}^{TZ} \neq Y_{d(i)}^{TZ}$, which allows us to assess possible changes in the shear-zone yield strength with time during a slip cycle. Specifically, we assume that the static strength applies for the inter-slip phase and the onset of the slow-slip phase, the dynamic strength applies for the slow-slip phase, and the locking strength applies only at the end of the slow-slip phase. If the static strength is greater than the locking strength, it means that the shear-zone strength has increased during the inter-slip phase.

Forces exerted on the transition-zone (TZ) block include (1) elastic force during the inter-slip phase (i.e., $F_{e(i)}^{TZ/IS}$ in Table 1) and the slow-slip phase (i.e., $F_{e(i)}^{TZ/SS}$ in Table 1), (2) frictional force (i.e., $F_{f(i)}^{TZ}$ in Table 1) during both the inter-slip and slow-slip phases along the basal slow-slip shear zone, (3) viscoplastic force (i.e., $F_{vp(i)}^{TZ}$ in Table 1) that operates only during the slow-slip phase, and (4) gravitational force induced by the weight of the TZ block along the inclined slow-slip shear zone (i.e., F_g^{TZ} in Table 1).

3. Mechanics of a slow-slip cycle

3.1. Inter-slip phase

Force balance of the transition-zone (TZ) block at the end of an inter-slip phase can be written as:

$$F_{e(i)}^{TZ/IS} \cos(\delta) + F_{f(i)}^{TZ} + F_g^{TZ} = 0 \tag{1}$$

where $F_{e(i)}^{TZ/IS}$ is the elastic force exerted on the transition-zone block during the inter-slip phase, $F_{f(i)}^{TZ}$ is the frictional force related to $\overline{\mu}_{s(i)}^{TZ}$, and F_g^{TZ} is the gravitational force induced by the weight of the transition-zone block on the inclined shear zone (Table 1). Here, we are concerned with force balance at the end of the inter-slip phase when the frictional strength is defined by the static friction. As we assume the slip magnitude is the same in every slip cycle, we have

$$\Delta x_{(i)}^{(2)} = \Delta x_{(i-1)}^{(2)} = \Delta x^{(2)},$$

$$\Delta T_{IS(i)} = \Delta T_{IS(i-1)},$$
$$\Delta x^{(2)} = \alpha_i \Delta x^{(1)}.$$

Noting the above relationships and considering equation (1) yield (*see supplemental materials for derivation*):

$$\Delta\overline{\mu}_{s(i)}^{TZ} = \left(\overline{\mu}_{s(i)}^{TZ} - \overline{\mu}_{s(i-1)}^{TZ}\right) = \frac{\Delta x_{(i)}^{(2)} \cos(\delta)\left(\frac{H'_2}{L_2}E_2 - \frac{H'_1}{\alpha_i L_1}E_1\right)}{\rho g H'_2 L_2} \tag{2}$$

In the above equation $\Delta\overline{\mu}_{s(i)}^{TZ} = 0$ if $\Delta x_{(i)}^{(2)} = 0$ and/or $\left(\frac{H'_2}{L_2}E_2 - \frac{H'_1}{\alpha_i L_1}E_1\right) = 0$. Here $\Delta x_{(i)}^{(2)} = 0$ means no incremental shortening in spring 2 during a slip cycle, which in turn requires no landward motion of the transition-zone (TZ) block at the end of a slow-slip cycle. This situation is incompatible with the fundamental observation of slow-slip events at convergent margins (Dragert et al., 2001).

We find that $\left(\frac{H'_2}{L_2}E_2 - \frac{H'_1}{\alpha_i L_1}E_1\right) \neq 0$ for all the subduction zones that we have examined (Table 2). Hence, the condition of landward motion as represented by $\Delta x_{(i)}^{(2)} > 0$ requires $\left(\frac{H'_2}{L_2}E_2 - \frac{H'_1}{\alpha_i L_1}E_1\right)$ and $\Delta\overline{\mu}_{s(i)}^{TZ}$ in equation (2) to have the same sign. This condition can be satisfied if

$$\Delta\overline{\mu}_{s(i)}^{TZ} < 0 \text{ (shear-zone weakening)} \quad \text{when } \alpha_i < \alpha_{cr} \tag{3a}$$
$$\Delta\overline{\mu}_{s(i)}^{TZ} > 0 \text{ (shear-zone strengthening)} \quad \text{when } \alpha_i > \alpha_{cr} \tag{3b}$$

where α_{cr} is the *critical strain partitioning coefficient* defined by

$$\alpha_{cr} = \frac{H'_1 L_2}{H'_2 L_1}\frac{E_1}{E_2} \tag{3c}$$

The above relationship indicates that α_{cr} depends on the size and elastic strength of the subduction system. As $\Delta x_{(i)}^{(2)}$ is an observable, the change in the frictional strength of the shear zone $\Delta\overline{\mu}_{s(i)}^{TZ}$ can be determined using equation (2). A special situation is

$$\Delta\overline{\mu}_{s(i)}^{TZ} = 0 \quad \text{when } \alpha_i = \alpha_{cr} \tag{4}$$

under which no landward motion is possible. An obvious implication of equation (4) is that shear-zone strengthening or weakening is a pre-requisite of slow-slip cycles.

As $\Delta\overline{\mu}_{s(i)}^{TZ}$ measures a change in the frictional strength of the slow-slip shear zone between two slip cycles, we refer to this quantity as *incremental strength change*. The subduction systems examined in this study all but one yield $\alpha_i > \alpha_{cr}$ (Table 2). The exception with $\alpha_i < \alpha_{cr}$ lacks constraints on the shear-zone thickness, so the result may not be reliable. In light of the $\alpha_i > \alpha_{cr}$ relationships shown in Table 2, it seems that deep slow-slip shear zones are dominated by strengthen hardening with time from one slow-slip cycle to the next, a possibility that was also raised by Peng and Rubin (2017) based on time-varying tremor migration rates and amplitudes in the Guerrero deep slow-slip shear zone of Mexico.

3.2. Slow-slip phase

Viscoplastic slow-slip shear zone. Viscoplastic constitutive equations assumed in this study is expressed as

$$\dot{\varepsilon}_{vp} = \frac{[V_{FW} \mp |\dot{X}_{(i)}(t')|]\cos(\delta)}{\Delta z} = \frac{(\tau_{vp} - Y_{d(i)}^{TZ})}{\eta_e} \quad \text{if } |\tau_{vp}| \geq Y_{s(i)}^{TZ} \tag{5a}$$

$$\dot{\varepsilon}_{vp} = \frac{[V_{FW} \mp |\dot{X}_{(i)}(t')|]\cos(\delta)}{\Delta z} = 0 \quad \text{if } |\tau_{vp}| < Y_{s(i)}^{TZ} \tag{5b}$$

Table 2
Estimated rheological properties from deep (15–50 km) subduction shear zones where deep slow-slip events were recorded generated.

Slow-slip events	V_{FW} (cm/yr)	L_1, L_2 (km)	H'_1, H'_2 (km)	Δz (km)	$S^{SS}_{TZ(i)}$ (cm)[b] $\Delta T^{SS}_{TZ(i)}$ (day)	$S^{IS}_{TZ(i)}$ (cm)[b] $\Delta T^{IS}_{TZ(i)}$ (day)	α_i, α_{cr} Strengthening: ($\alpha_i > \alpha_{cr}$) Weakening: ($\alpha_i < \alpha_{cr}$)	$\eta_e{}^c \times 10^{16}$ (Pa s)
2002 Guerrero, Mexico (1)[a]	5 (1, 18)	60, 150 (1)	12, 26 (1)	3 (2)	10, 195 (1)	20, 2460 (22, 23)	0.79, 0.58 ($\alpha_i > \alpha_{cr}$)	2.95
2006 Guerrero, Mexico (3)	5 (1, 18)	60, 150 (1)	12, 26 (1)	3 (2)	6, 180 (3)	Unknown	Unknown	4.14
Northern Cascadia (4, 5)	4 (5, 19)	50. 50 (6)	10, 35 (6)	4 (7, 8)	2, 14 (5, 6)	4.7, 420 (6)	1.23, 0.57 ($\alpha_i > \alpha_{cr}$)	2.22
2010 Manawatu, New Zealand (12, 13)	3.5 (9, 20)	178, 250 (12)	13, 43 (12, 13)	3 (10, 11)	27 (12, 13) 270 (13)	Unknown		2.87
1995–2004 events, New Zealand (9)	3.5 (9, 20, 24)	178, 250 (9, 12)	13, 43 (12, 13)	3 (10, 11)	2.5, 10 (9)	8.8, 923 (9)	2.43, 0.21 ($\alpha_i > \alpha_{cr}$)	1.24
2003 July–Dec. SW Japan (16, 17)	5 (17, 21)	200, 56 (16)	12, 28 (16)	5 (15)	11, 165 (16)			3.50
2004 February, SW Japan (16, 17)	5 (17, 21)	59, 41 (16, 17)	16, 47 (16, 17)	5 (15)	2, 6 (16, 17)			1.63
2001–2003 Shikoku, SW Japan (26)	5 (17, 21)	59, 41 (16, 17)	16, 47 (16, 17)	5 (15)	1.8, 12 (26)	2.5, 180 (27)	0.36, 0.12 ($\alpha_i > \alpha_{cr}$)	3.47
1997–2007 Ryukyu, Japan (25)	12.5 (25)	50,100 (25)	10, 30 (25)	4 (?)	5.5, 30 (25)	6.5, 190 (25)	0.15, 0.33 ($\alpha_i < \alpha_{cr}$) (?)	1.57 (?)

[a] (1) to (25) are the sources of information from which the model-input parameters were obtained. See supplemental materials for the corresponding references.
[b] Slow-slip magnitude $S^{SS}_{TZ(i)}$ is estimated from dislocation modeling of surface geodetic deformation induced by the slow slip events. The inter-slip magnitude $S^{IS}_{TZ(i)}$ is calculated using $S^{IS}_{TZ(i)} = V_{FW} \Delta T^{IS}_{TZ(i)}$, where V_{FW} is the footwall/subducting-slab velocity assumed to be the same as the plate convergence rate, and $\Delta T^{IS}_{TZ(i)}$ is the inter-slip duration.
[c] The estimated viscosity was calculated assuming the differential friction coefficient $\overline{\mu}^{TZ}_{(s-d)(i)} = 10^{-4}$ and Young's modulus $E_2 = 2E_1 = 30$ GPa.

where $\dot{\varepsilon}_{vp}$ and τ_{vp} are viscoplastic strain rate and stress, Δz is shear-zone thickness, and $X_i(t') = X_{(i)TZ}(t')$ is slow-slip history of the TZ block during a slow-slip phase. Note that $Y^{TZ}_{s(i)} > Y^{TZ}_{d(i)}$, which is consistent with the experimental results on viscoplastic deformation of crustal rocks under the brittle–ductile transition conditions (e.g., Pec et al., 2016). Also note that if the shear-zone shear stress τ_{vp} is similar in magnitude to that of the static yield strength of the shear zone $Y^{TZ}_{s(i)}$, a viscoplastic slow-slip event could occur under small stress perturbation as indicated by equation (5a). This shear-zone property may explain why some SSEs are sensitive to Earth tides (e.g., Hawthorne and Rubin, 2010).

The "$-$" sign is for forward motion of the transition-zone (TZ) block (Fig. 1c) and "$+$" sign for backward motion of the TZ block (Fig. 1d). The two modes of slow-slip can be differentiated by $|\tau_{vp}(t'=0)| = Y^{TZ}_{s(i)}$ required in the assumed constitutive relationship, which can be stated as

$$\eta_e > \eta^* \quad \text{for } \dot{X}_{(i)}(t'=0) > 0 \text{ forward motion} \tag{6a}$$

$$\eta_e = \eta^* \quad \text{for } \dot{X}_{(i)}(t'=0) = 0 \text{ no motion} \tag{6b}$$

$$\eta_e < \eta^* \quad \text{for } \dot{X}_{(i)}(t'=0) < 0 \text{ backward motion} \tag{6c}$$

where $\eta^* = \dfrac{\Delta z(Y^{TZ}_{s(i)} - Y^{TZ}_{d(i)})}{\cos(\delta) V_{FW}} = \dfrac{\Delta z(\Delta \overline{\mu}^{TZ}_{(s-d)(i)}) \rho g H'_2}{\cos(\delta) V_{FW}}$ is the *characteristic viscosity* of the shear zone, with $\Delta \overline{\mu}^{TZ}_{(s-d)(i)} \equiv (\overline{\mu}^{TZ}_{s(i)} - \overline{\mu}^{TZ}_{d(i)})$ as the *differential friction coefficient*. For unidirectional slow-slip motion, $\dot{X}_{(i)}(t'=0)$ and $\dot{X}_{(i)}(t'>0)$ have the same sign and thus (6a)–(6c) must hold for $t' > 0$.

The condition of $|\tau_{vp}(t'=0)| = Y^{TZ}_{s(i)}$ also yields an initial condition for the onset of viscoplastic deformation as:

$$\dot{X}_{(i)}(t'=0) = V_{cr(i)} = \pm \frac{\Delta \overline{\mu}^{TZ}_{(s-d)(i)} \rho g H'_2 \Delta z - \eta_e V_{FW}}{\cos(\delta) \eta_e} \tag{7}$$

where $V_{cr(i)}$ is the *characteristic velocity* of the slow-slip shear zone. Because $V_{cr(i)} < 10^{-7}$ m/s when $\Delta \overline{\mu}^{TZ}_{(s-d)(i)} = 10^{-4}$, $\rho = 3000$ kg/m^3, $g = 10$ m/s^2, $H'_2 = 30$ km, $\Delta z = 3$ km, $\eta_e = 10^{17}$ Pa s, and $V_{FW} = 40$ mm/yr, a typical set of model parameters for a D-SSE generating convergent margin (Table 2), we conclude that any initial unstable sliding of a slow-slip event due to a rate-weakening

process should be terminated nearly instantaneously once it starts. Note that $V_{cr(i)} \to \infty$ when $\eta_e \to 0$, which highlights the key role of viscous shear in stabilizing slow-slip motion.

Maximum stress drops. The stress drop of a slow-slip event can be obtained by the difference between the shear-zone stress prior to the slip event and the shear-zone stress during the slip event. This can be expressed equivalently as the difference between the static yield strength and the viscoplastic shear stress of the shear zone when $t' > 0$, which is

$$\begin{aligned} \Delta \sigma_{drop(i)}(t') &= \left(Y^{TZ}_{s(i)} - \tau_{vp(i)}(t')\right) \\ &= \Delta \overline{\mu}^{TZ}_{(s-d)(i)} \rho g H'_2 \cos(\delta) \\ &\quad - \frac{\eta_e[V_{FW} \pm |\dot{X}(t')|] \cos(\delta)}{\Delta z} \end{aligned} \tag{8a}$$

Removing the time-dependent term in the above equation, we obtain the maximum stress drop as

$$\Delta \sigma_{drop(i)\_max} = \Delta \overline{\mu}^{TZ}_{(s-d)(i)} \rho g H'_2 \cos(\delta) \tag{8b}$$

For the maximum stress drops of $\Delta \sigma_{drop(i)\_max} = 10$–100 kPa associated with slow-slip events (e.g., Ide et al., 2007b), it requires the maximum differential friction $\Delta \overline{\mu}^{TZ}_{(s-d)(i)} = 10^{-4}$ to 10^{-5} assuming $\rho = 3000$ kg/m^3, $g = 10$ m/s^2, $H'_2 = 30$ km (a good approximation for all the slow-slip shear zones listed in Table 2), and $\cos(\delta) = 1$ (good approximation for low-angle subduction zones such as the Cascadia margin).

Slow-slip history. Newton's second law for forces exerted on the transition-zone (TZ) block *during its slow-slip history* yields:

$$\begin{aligned} F^{spring\frac{1}{SS}}_{e(i)} + F^{spring\frac{2}{SS}}_{e(i)} + F^{TZ}_{vp(i)} + F^{TZ}_g \\ = \ddot{X}_{(i)}(t') \rho H'_2 L_2 W(t') \cos(\delta) \end{aligned} \tag{9a}$$

where $X_{(i)}(t') = X_{TZ(i)FWD/BWD}(t')$ represents the forward and backward slow-slip history of the TZ block. The above equation has the form of

$$\ddot{X}_{(i)}(t') + b\dot{X}_{(i)}(t) + cX_{(i)}(t') = d_0 + d_1 t' \tag{9b}$$
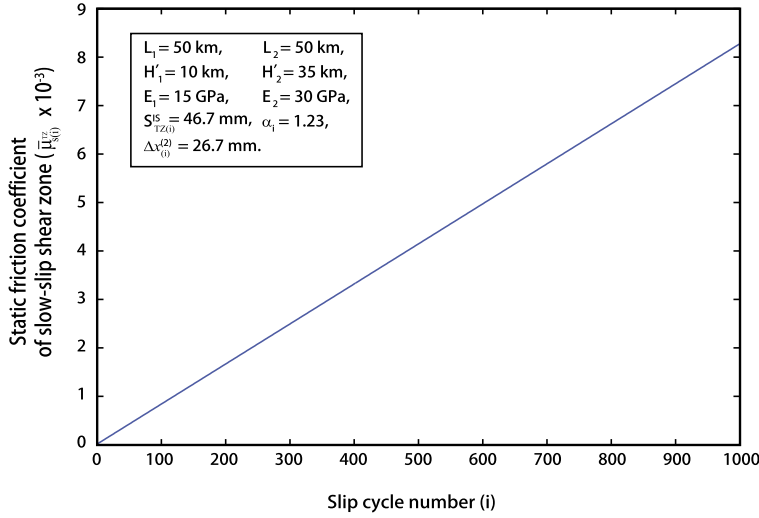
Fig. 3. Increasing effective coefficient of static friction of a slow-slip shear zone with the number of slow-slip cycles. Note that the true values of the coefficient friction are the numbers listed on the left side of the vertical axis that time 10^{-3}. Model parameters are from the Cascadia listed in Table 2.

where b, c, d_0, and d_1 are constants; their derivation can be found in *the supplemental materials* whereas their values are listed in Table 1. The above equation has three possible solutions: (i) with two imaginary roots when $\eta_e < \eta_{cr}$, (ii) with two repeating real roots when $\eta_e = \eta_{cr}$, and (iii) with two different real roots when $\eta_e > \eta_{cr}$. Here, η_{cr} is the *critical viscosity* of the shear zone (not be confused with the *characteristic viscosity* η^* defined above) defined by

$$\eta_{cr} = 2\Delta z \rho H_2' \cos(\delta) \sqrt{\left(\frac{H_1'}{L_1}E_1 + \frac{H_2'}{L_2}E_2\right)\frac{1}{\rho H_2' L_2}} \quad (10)$$

We rule out $\eta_e < \eta_{cr}$ as it requires oscillation of the transition-zone block (such a solution is obtained by Hayman and Lavier, 2014), which is inconsistent with the net landward motion of the transition-zone block after a full slow-slip cycle (e.g., Dragert et al., 2001) (Fig. 1d). The case of $\eta_e = \eta_{cr}$ requires $\eta_e = 10^{10}$–10^{12} Pa s for the Circum-Pacific D-SSE shear zones using the model parameters in Table 2, which is 5–7 orders of magnitude lower than the estimated subduction-zone viscosities ($\geq 10^{17}$ Pa s) using other independent means (e.g., Wang et al., 2012; Hu et al., 2016). Hence, we consider below only the solution with two real roots, which can be written as

$$X(t') = \left\{ C_1 \exp\left[t'\frac{(-\sqrt{b^2 - 4c} - b)}{2}\right] \right.$$
$$\left. + C_2 \exp\left[t'\frac{(\sqrt{b^2 - 4c} - b)}{2}\right] \right\} + \frac{d_0}{c} - \frac{bd_1}{c^2} + \frac{d_1}{c}t' \quad (11)$$

where C_1 and C_2 are determined by the initial conditions of $X_{(i)}(t' = 0) = 0$ and $\dot{X}_{(i)}(t' = 0) = V_{cr(i)}$, and their values are listed in Table 1.

We assign a locking strength for the slow-slip shear zone, $Y_{L(i)}^{TZ} = \overline{\mu}_{L(i)}^{TZ} \rho g H_2' \Delta z$, to terminate a slow-slip event at the time of $t' = \Delta T_{TZ(i)}^{SS}$, which can be expressed by a locking velocity defined as,

$$\dot{X}_{(i)}\left(t' = \Delta T_{TZ(i)}^{SS}\right) = V_{L(i)} = \pm\frac{(\overline{\mu}_{L(i)}^{TZ} - \overline{\mu}_{d(i)}^{TZ})\rho g H_2' \Delta z - \eta_e V_{FW}}{\eta_e} \quad (12)$$

Here $\overline{\mu}_{L(i)}^{TZ}$ is the effective coefficient of "locking friction", similar in concept to the "arrest frictional strength" of Ben-Zion (2012).

When $(\overline{\mu}_{s(i)}^{TZ} - \overline{\mu}_{d(i)}^{TZ}) = 10^{-4}$, as constrained by the highest stress-drop magnitudes of 100 kPa discussed above, we find that $(\overline{\mu}_{L(i)}^{TZ} - \overline{\mu}_{d(i)}^{TZ}) \approx 10^{-7}$, or $\overline{\mu}_{s(i)}^{TZ} \approx \overline{\mu}_{L(i)}^{TZ}$ using the model parameters listed in Table 2. This means that the frictional strength of the slow-slip shear zone recovers to nearly its starting static strength after a slow-slip event when the observed maximum stress drops are used.

4. Model results

Our mechanical analyses yield seven model parameters that govern the mechanical behaviors of an idealized convergent margin (Table 1):

(1) the *strain partitioning coefficient* $\alpha_i = \frac{\Delta x_i^{(2)}}{\Delta x_i^{(1)}}$, which quantifies the elastic strain gradient across a forearc and predicts a possible coseismic-slip distribution during a megathrust event: overshooting when $\alpha_i < 1$ and undershooting when $\alpha_i > 1$.

(2) the *critical strain partitioning coefficient* $\alpha_{cr} = \frac{H_1' L_2}{H_2' L_1}\frac{E_1}{E_2}$, which can be used to assess whether a slow-slip shear zone has evolved through a strength-hardening or strength-weakening process when compared against the observationally determined *strain partitioning coefficient* α_i;

(3) the *characteristic viscosity* $\eta^* = \frac{\Delta z(\Delta \overline{\mu}_{(s-d)(i)}^{TZ})\rho g H_2'}{\cos(\delta)V_{FW}}$, which can be used to determine whether a slow-slip shear zone favors forward ($\eta_e < \eta^*$) or backward ($\eta_e > \eta^*$) slow-slip motion when compared against the effective viscosity of the shear zone η_e;

(4) the *critical viscosity* $\eta_{cr} = 2\Delta z \rho H_2' \cos(\delta)\sqrt{\left(\frac{H_1'}{L_1}E_1 + \frac{H_2'}{L_2}E_2\right)\frac{1}{\rho H_2' L_2}}$, which governs whether oscillatory motion ($\eta_e < \eta_{cr}$) or exponentially decayed slow-slip motion ($\eta_e > \eta_{cr}$) would operate in a forearc region;

(5) the *characteristic velocity* $V_{cr(i)} = \pm\frac{\Delta \overline{\mu}_{(s-d)(i)}^{TZ}\rho g H_2' \Delta z - \eta_e V_{FW}}{\cos(\delta)\eta_e}$, which governs the initiation of slow-slip motion;

(6) the *locking velocity* $V_{L(i)} = \pm\frac{(\overline{\mu}_{L(i)}^{TZ} - \overline{\mu}_{d(i)}^{TZ})\rho g H_2' \Delta z - \eta_e V_{FW}}{\eta_e}$, which governs the termination of slow-slip motion; and

(7) the *incremental strength change* $\Delta\overline{\mu}_{s(i)}^{TZ} = \frac{\Delta x_i^{(2)}\cos(\delta)(\frac{H_2'}{L_2}E_2 - \frac{H_1'}{\alpha_i L_1}E_1)}{\rho g H_2' L_2}$, which can be used to quantify the magnitude of shear-zone hardening ($\Delta\overline{\mu}_{s(i)}^{TZ} > 0$) or weakening ($\Delta\overline{\mu}_{s(i)}^{TZ} < 0$) using geode-

tic observation $\Delta x_{(i)}^{(2)}$ and the geometric and mechanical properties of the idealized convergent system.

In order to invert for the effective viscosity of a deep slow-slip shear zone at a convergent margin, we need to have the following parameters as model input: plate velocity (V_{FW}), geodetically determined slow-slip and inter-slip motion and duration ($S_{TZ(i)}^{SS}$, $S_{TZ(i)}^{IS}$, $T_{TZ(i)}^{SS}$, and $\Delta T_{TZ(i)}^{IS}$), seismically determined shear-zone thickness (Δz), seismogenic and slow-slip shear-zone lengths (L_1, L_2), shear-zone depths (H_1', H_2'), and shear-zone dip angle (δ). Their values are listed in Table 2 and the sources of references can be found in the *supplemental materials*. For the model results shown in Figs. 3, 4 and 5, we use model parameters from the Cascadia margin and assume Young's moduli of the two springs as $E_2 = 2E_1 = 15$ GPa, which are commonly accepted values for crustal rocks (e.g., Hu et al., 2016). The assumption of $E_2 = 2E_1$ is to show that the central forearc is generally stronger with crystalline basement rocks than the frontal forearc composed mostly of weak mélange materials (e.g., Wakabayashi, 2015). We assume $\Delta \overline{\mu}_{(s-d)(i)}^{TZ} = 10^{-5}$ to 10^{-4} as constrained by the maximum stress drops associated with slow-slip events as mentioned above.

The effective coefficient of static friction, $\overline{\mu}_{s(i)}^{TZ}$, may increase with time when $\alpha_i > \alpha_{cr}$ (Fig. 3). The change in $\overline{\mu}_{s(i)}^{TZ}$ may result from shear-zone strengthening as observed from direct field measurements (e.g., Xue et al., 2013) and demonstrated in laboratory experiments (Yasuhara et al., 2005). In this context, our model relates geodetic observables to the incremental change in frictional strength $\Delta \overline{\mu}_{(s)(i)}^{TZ}$ when the relationship in equation (2) is used.

Using model parameters from the Cascadia margin, we show that the *total* slow-slip magnitude $S_{TZ(i)}^{SS}$ increases with increasing $\Delta \overline{\mu}_{(s-d)(i)}^{TZ}$ and decreases with increasing η_e (Fig. 4a). Because $\eta_e \sim \exp(\frac{E}{RT})$ for a thermally activated frictional/shear process (E is activation energy and R universal gas constant) (e.g., Chester, 1994), the relationship in Fig. 4a implies that slow-slip events produce larger slip magnitudes along a warm (low-viscosity) slow-slip shear zone. This prediction is consistent with the observations from the Nankai and Cascadia subduction zones (Wang et al., 2008).

Fig. 4b shows that the larger the viscosity the longer a slow-slip event lasts. This result implies a warm subduction zone and the deeper/warmer section of a slow-slip shear zone should host more frequent and shorter-duration slow-slip events, consistent with the current knowledge on the spatial and temporal evolution of slow-slip events and episodic tremors at convergent margins (e.g., Wang et al., 2008; Obara and Kato, 2016; Gao and Wang, 2017). Note that the recurrence time of a cyclic slow-slip sequence depends not only on the viscosity and differential friction, but also on the *strengthen increment* $\Delta \overline{\mu}_{(s)(i)}^{TZ}$ between slip cycles (Fig. 4c).

The detailed slip history of a slow-slip event is highly sensitive to η_e, expressed by a faster drop in slip rate with time when the shear-zone viscosity is low (Fig. 5a). Applying this result against the geodetic data from the 2009 Cascadia slow-slip event (Figs. 5b–5e) (e.g., Bartlow et al., 2011), a northward decrease in the slow-slip shear-zone viscosity can be inferred (Fig. 5f). Although the inference is consistent with the northward decreasing age of the subducting oceanic crust (Wilson, 1993), which requires a northward increase in the subduction shear-zone temperature and a northward decrease in shear-zone viscosity, this interpretation is only qualitative as our model assumes uniform vertical deformation that overestimates the surface slip magnitudes by a factor of ~4 (e.g., Dragert et al., 2001). Fig. 5a shows how the viscosity decides forward vs. backward slow-slip as outlined in equations (6a), (6b), and (6c). Note that the upward limit for the slip rate of a forward slow-slip event is the footwall velocity; that is, $\dot{X}_{FWD}(t')|_{\eta_e > \eta_*} < V_{FW}$.
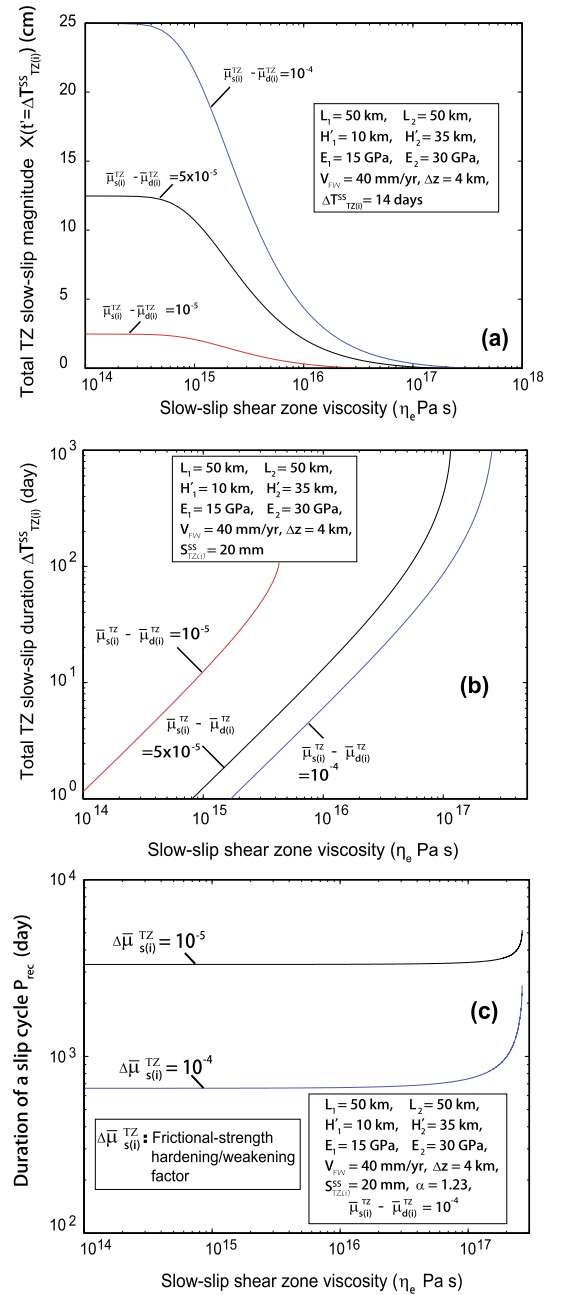

Fig. 4. (a) The total slow-slip magnitude of the transition-zone (TZ) block after the completion of a slow-slip cycle as a function of the effective shear-zone viscosity η_e with variable differential friction coefficient $\Delta \overline{\mu}_{(s-d)(i)}^{TZ}$. Here, $S_{TZ(i)}^{SS}$ is the total slow-slip magnitude and $X(t')$ is slow-slip history; they are related by $X(t' = \Delta T_{TZ(i)}^{SS}) = S_{TZ(i)}^{SS}$, where $\Delta T_{TZ(i)}^{SS}$ is the total duration of the slow-slip phase. (b) The total slow-slip phase duration of the transition-zone (TZ) block, $\Delta T_{TZ(i)}^{SS}$, as a function of the effective shear-zone viscosity η_e with varying differential friction coefficient $\Delta \overline{\mu}_{(s-d)(i)}^{TZ}$. (c) Periodicity of a cyclic slow-slip sequence as a function of the effective shear-zone viscosity η_e and the incremental strengthen change $\Delta \overline{\mu}_{s(i)}^{TZ}$. The quantity, $\Delta \overline{\mu}_{s(i)}^{TZ}$, which measures the incremental increase/decrease in the magnitude of static shear-zone effective friction coefficient between two slow-slip cycles, should not be confused with the differential friction coefficient, $\Delta \overline{\mu}_{(s-d)(i)}^{TZ}$, which measures the reduction in the effective friction coefficient from a value at the onset of a slow-slip phase to that during the main slow-slip phase.

The estimated strain partitioning coefficients α_i and the effective shear-zone viscosity for several slow-slip convergent margins are summarized in Table 2. The shear-zone viscosity is on the order of ~10^{16} Pa s, whereas the estimated α_i values vary from 0.15 to 2.43. Among the five convergent margins examined in this
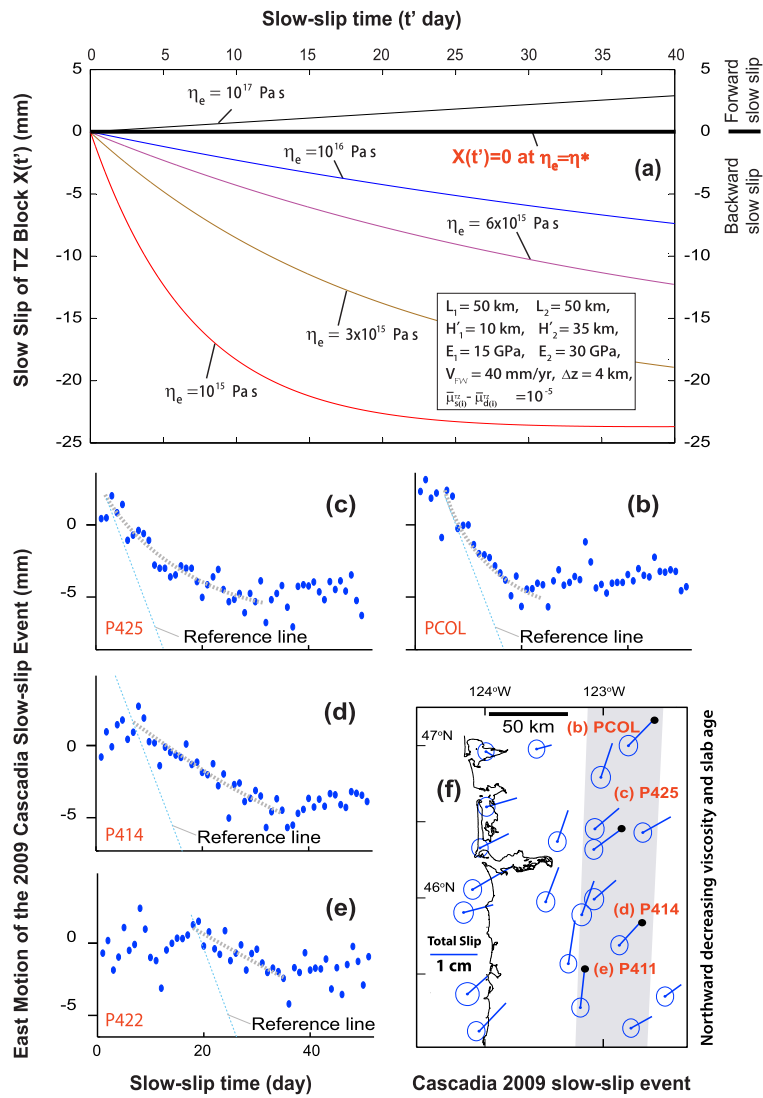
Fig. 5. (a) Slow-slip history of the transition-zone (TZ) block as a function of the effective shear-zone viscosity η_e. Note that the initial slip rate decreases more rapidly with time for a lower effective shear-zone viscosity than that for a higher effective shear-zone viscosity. Also note that $X(t') > 0$ for forward slow-slip motion with a high effective shear-zone viscosity and $X(t') < 0$ for backward slow-slip motion at the Cascadia forearc, with a lower effective shear-zone viscosity. (b)–(e) Eastward motion histories of selected GPS stations located along the north-striking Cascadia forearc during the 2009 slow-slip event. See (f) for locations of the GPS stations and the total slip during the slow-slip event for all the GPS stations in the region (modified from Bartlow et al., 2011). Note that the best fitting lines drawn by hand (gray dashed lines) display a northward increase in the initial slope of the slip-history curves visibly by comparing against the reference slope lines shown as thin blue dashed straight lines. When comparing the results shown in Fig. 5a above, the GPS slip histories require a northward decrease in the Cascadia deep slow-slip shear-zone viscosity. (For interpretation of the colors in the figure(s), the reader is referred to the web version of this article.)

study, four yield $\alpha_i > \alpha_{cr}$ that correspond to strength hardening and one yields $\alpha_i < \alpha_{cr}$ that corresponds to strength weakening of the slow-slip shear zones. When estimated α_i values are plotted against the estimated shear-zone viscosity, we find that α_i decreases linearly with viscosity for the strength-hardening slow-slip shear zones (Fig. 6). Because decreasing α_i corresponds to increasing elastic strain in the seismogenic segment closest to the trench, the plot in Fig. 6 shows that a higher elastic force in the frontal-most forearc requires a higher viscous shear stress to counterbalance this force in the slow-slip shear zone below the transition block. It is interesting to note that the only strengthen-weakening shear zone is plotted outside this trend.

5. Discussion

Our model assumes that a forearc region can be discretized, which may overlook the role of continuum deformation in controlling the hanging-wall response to a slow-slip event. Our kinematic

model in Fig. 2 assumes that a single megathrust event ruptures both the seismogenic fault and slow-slip shear zone. In reality, the rupture of the two zones may be accomplished by a cluster of large slow-slip events either prior to a megathrust event along the seismogenic zone, or more likely afterwards through afterslip deformation (e.g., Hu et al., 2016; Gao and Wang, 2017). Note that our analyses on the inter-slip and slow-slip mechanics do not rely on this assumption. Below we list major results of our model and discuss their implications.

Our model shows that a change in the shear-zone yield strength during the inter-slip phase is a pre-requisite for the occurrence of slow-slip events. Because of this, the magnitude of the *incremental strength change* of a slow-slip shear zone can be determined by geodetic observations (see equation (2) and Table 1).

When the continental interior is fixed, a slow-slip event could be accommodated by landward motion (Fig. 1c) when the slow-slip shear zone is partially coupled, allowing the hanging wall moving forward but at a slower rate than the footwall speed. This mode of
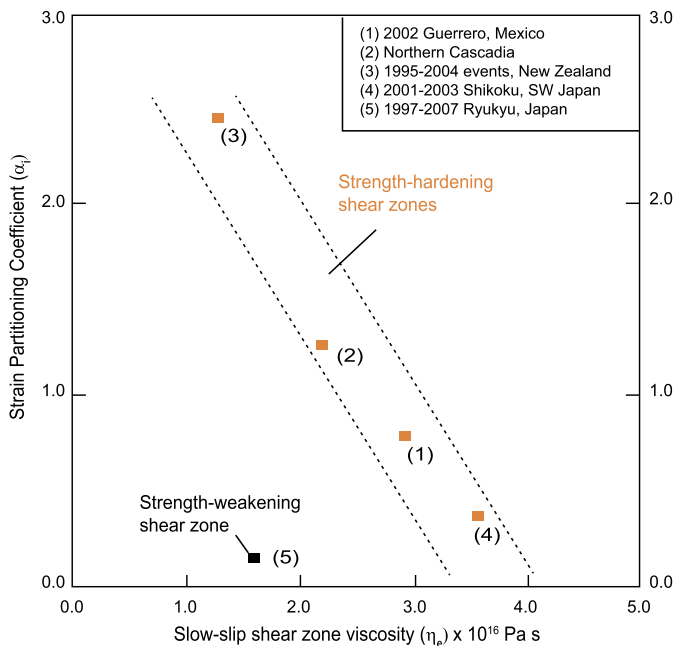
Fig. 6. A plot of the estimated strain partitioning coefficients and the estimated effective shear-zone viscosities from the convergent margins examined in this study (see Table 2). Note that the effective viscosity decreases linearly with the strain partitioning coefficient for strength-hardening deep slow-slip shear zones shown as red dots, which is explained as a result of balance between the elastic and viscoplastic forces in the slow-slip generating subduction systems. The single strength-weakening data point is shown as a black dot.

slow slip can be achieved only if the shear-zone viscosity is greater than a characteristic value that is inherently a combined geometric and mechanical property of the subduction system (see equations (6a)–(6c)). The lack of documented forward slow-slip events in nature at convergent margins places an upper bound on the shear-zone viscosity (Fig. 5a).

The magnitude, duration, and recurrence time of cyclic slow-slip events depend critically on the shear-zone viscosity. As viscosity decreases exponentially with temperature, our model provides a physical explanation for why more frequent slow-slip events with shorter durations occur at warmer convergent margins and along the deeper/warmer section of a deep slow-slip shear zone (e.g., Wang et al., 2008; Obara and Kato, 2016; Gao and Wang, 2017). Our model results also show that the slip-rate history of a slow-slip event is sensitive to the shear-zone viscosity: a slow rate for a high-viscosity shear zone and a fast rate for a low-viscosity shear zone.

Should unstable sliding occur at the onset of a slow-slip event, it must terminate nearly instantaneously if the slow-slip shear zone deforms viscoplastically, as the characteristic velocity sets the upper limit of a possibly runaway velocity on the order of $<10^{-7}$ m/s using the range of reasonable model parameters. Additionally, using the slow-slip magnitudes and durations and the known geometric and kinematic parameters of D-SSE generating convergent margins, our model yields order-of-magnitude estimates of shear-zone viscosity of $\sim 10^{16}$ Pa s. This value is lower than 10^{17}–10^{19} Pa s determined from post-seismic deformation of the same margins that we have investigated (e.g., Wang et al., 2012; Hu et al., 2016). The discrepancy can be reconciled by the fact that post-seismic deformation results from motion along the much stronger seismogenic faults and flow from the stronger mantle wedges (Wang et al., 2012; Hu et al., 2016).

The absence of geodetically detectable D-SSEs at some convergent margins such as South America (Feng et al., 2015; Obara and Kato, 2016) was explained by the lack of high pore-fluid pressure in the existing literature (e.g., Audet and Schwartz, 2013). However, this explanation alone has been shown to be inconsistent with the low vp/vs data indicating high pore-fluid pressure at the convergent margins where D-SSEs are absent (Hicks et al., 2014). Using our model, the above discrepancy could be reconciled if the shear-zone viscosity is (i) equal to its characteristic viscosity ($\eta_e = \eta^*$) as shown in Fig. 5a, or (ii) so high that the recurrence time interval is longer than the duration of available geodetic observations (Fig. 4b). It is also possible that the occurrence of D-SSEs depends on a specific relationship between the shear-zone yield strengths and the fluctuating shear-zone stress associated with the elastic loading. According to the conceptual model shown in Fig. 7, transient slow-slip events can only occur when the shear zone is alternately locked and unlocked, possibly controlled by the proportionality of the rigid blocks/mineral phases and their ductile creeping matrix. In other words, only when the interseismic stress fluctuates between the static and dynamic yield strengths of the shear zone can episodic slow-slip events occur during each slip cycle.

6. Conclusions

Our viscoplastic model provides a rate-strengthening mechanism for stabilizing initially unstable sliding of deep (15–50 km) slow-slip events (D-SSEs) at convergent margins. The assumed viscoplastic rheology is consistent with recent advances in field observations, laboratory experiments, and thermomechanical modeling relevant to D-SSE studies. The well-established segmentation of slip modes in the downdip direction of a subduction shear zone leads to discretization of a forearc region into three rigid blocks linked by two springs. This simplification leads to seven key model parameters that dictate a wide range of mechanical behaviors of an idealized convergent margin as summarized in Table 1. Key insights gained from this study are summarized below.

(1) The viscoplastic rheology requires the initially unstable sliding to be terminated at a *characteristic velocity* on the order of $<10^{-7}$ m/s, during which friction in the shear zone switches from rate-weakening to rate-strengthening. The characteristic velocity depends on the geometry and mechanical properties of the idealized subduction system.

(2) A deep slow-slip cycle can be expressed in two modes: alternating fast and slow landward motion, or alternating landward and trenchward motion relative to the fixed continental interior. The slip-mode selection depends on whether the effective shear-zone viscosity η_e is greater or smaller than the characteristic viscosity η^*, which is a function of the geometric and mechanical properties of the idealized subduction system.

(3) The spatial gradient of interseismic elastic strain across a forearc region can be quantified by strain partitioning coefficient α_i, which predicts whether overshooting ($\alpha_i < 1$) or undershooting ($\alpha_i > 1$) may occur during a megathrust event.

(4) Frictional strength hardening of a slow-slip shear zone during the inter-slip phase is a prerequisite for successive landward motion of a forearc region during cyclic slow-slip events. Without the strengthen hardening, the forearc region would stay stationary (see equation (2)).

(5) The magnitude, duration, and recurrence time of an interseismic cyclic slow-slip sequence depend on the geometry and mechanical properties of a subduction system. Using the slow-slip magnitudes and durations and the known geometric and kinematic parameters of convergent margins, our model yields order-of-magnitude estimates of viscosity at $\sim 10^{16}$ Pa s for D-SSE shear zones. As the effective viscosity of a slow-slip shear zone decreases exponentially with increasing temperature, our model provides a physical explanation for why more frequent and shorter durations
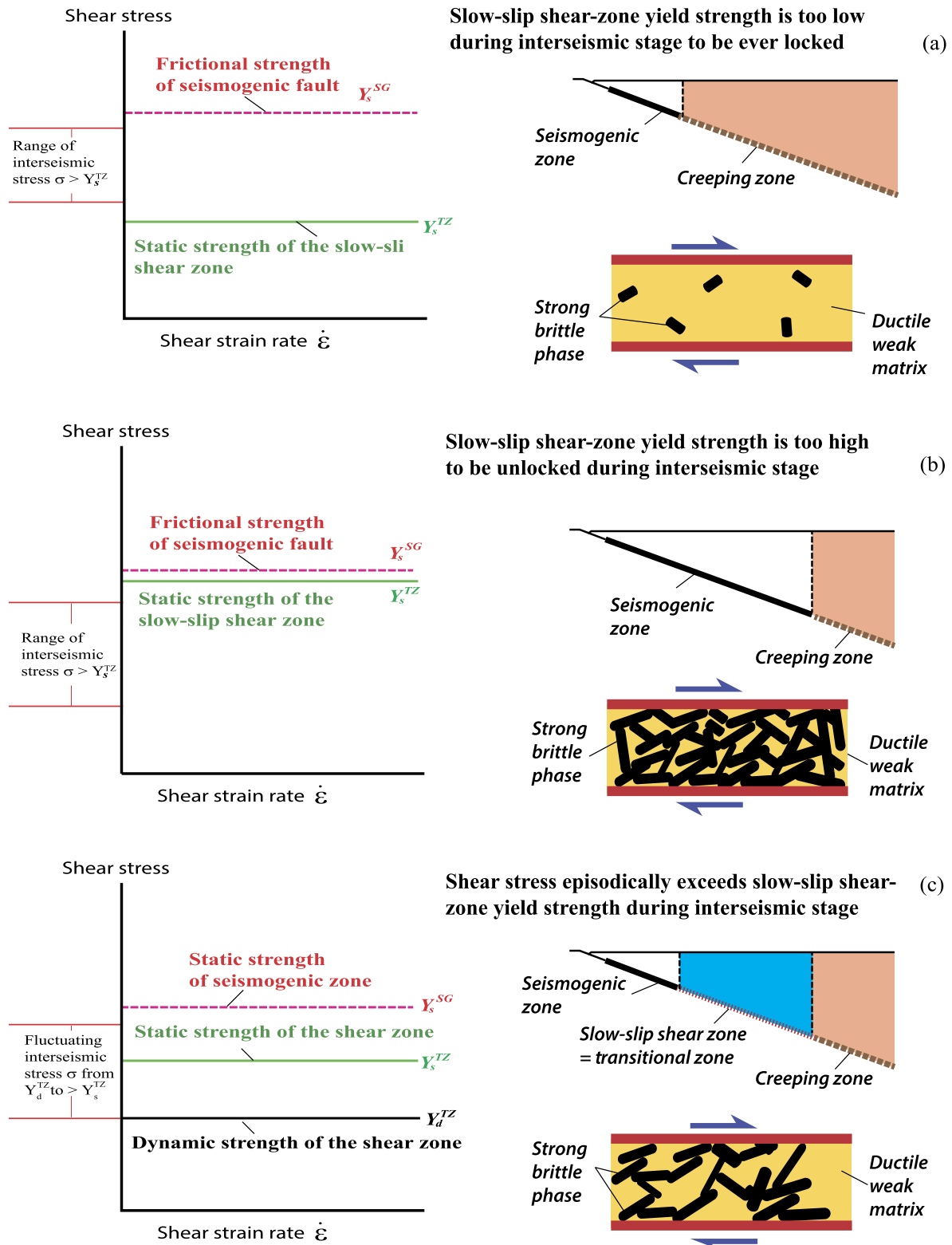
Fig. 7. Three possible situations of deep (15–50 km) subduction shear zones at the brittle–ductile transition depths due to different proportions of strong brittle blocks vs. weak ductile matrix: (a) interseismic shear-zone stress is always higher than the shear-zone static yield strength, which represents the case of a stable creeping shear zone and the brittle–ductile transition shear zone is merged with the ductile aseismic creeping zone; (b) interseismic shear-zone stress is always below the static yield strength and only exceeds it during a megathrust event, which represents the case of a interseismically locked brittle–ductile transition shear zone that is merged with the up-dip seismogenic fault; (c) interseismic shear-zone stress driven by elastic loading fluctuates between the dynamic and static yield strengths of a subduction shear zone at the brittle–ductile transition depths, causing the shear zone to be alternately locked and unlocked and thus occurrences of episodic deep slow-slip events.

of slow-slip events occur at warmer convergent margins and along the deeper section of a deep slow-slip shear zone.

(6) When estimated strain partitioning coefficient α_i is plotted against the estimated shear-zone viscosity for the convergent margins examined in this study, we find that α_i decreases linearly with viscosity for the strength-hardening slow-slip shear zones. This may be explained as a result of balance between the elastic and viscoplastic forces in the subduction system.

(7) Conceptually, our model implies that deep slow-slip events can only occur when the interseismic stress fluctuates between the static and dynamic yield strengths of a subduction shear zone at the brittle–ductile transition depths.

Acknowledgements

Appendix A. Supplementary material

Supplementary material related to this article can be found online at https://doi.org/10.1016/j.epsl.2018.02.042.

References

Angiboust, S., Kirsch, J., Oncken, O., Glodny, J., Monié, P., Rybacki, E., 2015. Probing the transition between seismically coupled and decoupled segments along an ancient subduction interface. Geochem. Geophys. Geosyst. 16 (6), 1905–1922.

Araki, E., Saffer, D.M., Kopf, A.J., Wallace, L.M., Kimura, T., Machida, Y., Ide, S., Davis, E., Expedition, I.O.D.P., 2017. Recurring and triggered slow-slip events near the trench at the Nankai Trough subduction megathrust. Science 356 (6343), 1157–1160.

Audet, P., Bürgmann, R., 2014. Possible control of subduction zone slow-earthquake periodicity by silica enrichment. Nature 510 (7505), 389.

Audet, P., Schwartz, S.Y., 2013. Hydrologic control of forearc strength and seismicity in the Costa Rican subduction zone. Nat. Geosci. 6 (10), 852–855.

Bartlow, N.M., Miyazaki, S.I., Bradley, A.M., Segall, P., 2011. Space-time correlation of slip and tremor during the 2009 Cascadia slow slip event. Geophys. Res. Lett. 38 (18).

Ben-Zion, Y., 2012. Episodic tremor and slip on a frictional interface with critical zero weakening in elastic solid. Geophys. J. Int. 189 (2), 1159–1168.

Brodsky, E.E., Mori, J., 2007. Creep events slip less than ordinary earthquakes. Geophys. Res. Lett. 34 (16), L16309. https://doi.org/10.1029/2007GL030917.

Chester, F.M., 1994. Effects of temperature on friction: constitutive equations and experiments with quartz gouge. J. Geophys. Res., Solid Earth 99 (B4), 7247–7261.

Dragert, H., Wang, K., James, T.S., 2001. A silent slip event on the deeper Cascadia subduction interface. Science 292 (5521), 1525–1528.

Feng, L., Hill, E.M., Banerjee, P., Hermawan, I., Tsang, L.L., Natawidjaja, D.H., Suwargadi, B.W., Sieh, K., 2015. A unified GPS-based earthquake catalog for the Sumatran plate boundary between 2002 and 2013. J. Geophys. Res., Solid Earth 120 (5), 3566–3598.

Gao, X., Wang, K., 2017. Rheological separation of the megathrust seismogenic zone and episodic tremor and slip. Nature 543 (7645), 416–419.

Grove, M., Bebout, G.E., Jacobson, C.E., Barth, A.P., Kimbrough, D.L., King, R.L., Zou, H., Lovera, O.M., Mahoney, B.J., Gehrels, G.E., 2008. The Catalina Schist: evidence for middle cretaceous subduction erosion of southwestern North America. In: Geological Society of America Special Papers, vol. 436, pp. 335–361.

Hawthorne, J.C., Rubin, A.M., 2010. Tidal modulation of slow slip in Cascadia. J. Geophys. Res., Solid Earth 115 (B9).

Hayman, N.W., Lavier, L.L., 2014. The geologic record of deep episodic tremor and slip. Geology 42 (3), 195–198.

He, C., Wang, Z., Yao, W., 2007. Frictional sliding of gabbro gouge under hydrothermal conditions. Tectonophysics 445 (3), 353–362.

He, C., Luo, L., Hao, Q.M., Zhou, Y., 2013. Velocity-weakening behavior of plagioclase and pyroxene gouges and stabilizing effect of small amounts of quartz under hydrothermal conditions. J. Geophys. Res., Solid Earth 118 (7), 3408–3430.

Hicks, S.P., Rietbrock, A., Ryder, I.M., Lee, C.S., Miller, M., 2014. Anatomy of a megathrust: the 2010 M8. 8 Maule, Chile earthquake rupture zone imaged using seismic tomography. Earth Planet. Sci. Lett. 405, 142–155.

Hu, Y., Bürgmann, R., Uchida, N., Banerjee, P., Freymueller, J.T., 2016. Stress-driven relaxation of heterogeneous upper mantle and time-dependent afterslip following the 2011 Tohoku earthquake. J. Geophys. Res., Solid Earth 121 (1), 385–411.

Huang, Y., Ampuero, J.P., Kanamori, H., 2014. Slip-weakening models of the 2011 Tohoku-Oki earthquake and constraints on stress drop and fracture energy. Pure Appl. Geophys. 171 (10), 2555–2568.

Ide, S., Shelly, D.R., Beroza, G.C., 2007a. Mechanism of deep low frequency earthquakes: further evidence that deep non-volcanic tremor is generated by shear slip on the plate interface. Geophys. Res. Lett. 34 (3), L03308. https://doi.org/10.1029/2006GL028890.

Ide, S., Beroza, G.C., Shelly, D.R., Uchide, T., 2007b. A scaling law for slow earthquakes. Nature 447 (7140), 76–79.

Ide, S., Baltay, A., Beroza, G.C., 2011. Shallow dynamic overshoot and energetic deep rupture in the 2011 Mw 9.0 Tohoku-Oki earthquake. Science 332 (6036), 1426–1429.

Ito, Y., Hino, R., Kido, M., Fujimoto, H., Osada, Y., Inazu, D., Ohta, Y., Iinuma, T., Ohzono, M., Miura, S., Mishina, M., 2013. Episodic slow slip events in the Japan subduction zone before the 2011 Tohoku-Oki earthquake. Tectonophysics 600, 14–26.

Kato, A., Obara, K., Igarashi, T., Tsuruoka, H., Nakagawa, S., Hirata, N., 2012. Propagation of slow slip leading up to the 2011 Mw 9.0 Tohoku-Oki earthquake. Science 335 (6069), 705–708.

Lavier, L.L., Bennett, R.A., Duddu, R., 2013. Creep events at the brittle ductile transition. Geochem. Geophys. Geosyst. 14 (9), 3334–3351.

Liu, Y., Rice, J.R., 2007. Spontaneous and triggered aseismic deformation transients in a subduction fault model. J. Geophys. Res., Solid Earth 112 (B9). https://doi.org/10.1029/2007JB004930.

Liu, Y., 2013. Numerical simulations on megathrust rupture stabilized under strong dilatancy strengthening in slow slip region. Geophys. Res. Lett. 40 (7), 1311–1316.

Nakata, R., Ando, R., Hori, T., Ide, S., 2011. Generation mechanism of slow earthquakes: numerical analysis based on a dynamic model with brittle–ductile mixed fault heterogeneity. J. Geophys. Res., Solid Earth 116 (B8).

Obara, K., Kato, A., 2016. Connecting slow earthquakes to huge earthquakes. Science 353 (6296), 253–257.

Peacock, S.M., Christensen, N.I., Bostock, M.G., Audet, P., 2011. High pore pressures and porosity at 35 km depth in the Cascadia subduction zone. Geology 39 (5), 471–474.

Pec, M., Stünitz, H., Heilbronner, R., Drury, M., 2016. Semi-brittle flow of granitoid fault rocks in experiments. J. Geophys. Res., Solid Earth 121, 1677–1705. https://doi.org/10.1002/2015JB012513.

Peng, Y., Rubin, A.M., 2017. Intermittent tremor migrations beneath Guerrero, Mexico, and implications for fault healing within the slow slip zone. Geophys. Res. Lett. 44 (2), 760–770.

Poulet, T., Veveakis, E., Regenauer-Lieb, K., Yuen, D.A., 2014. Thermo-poro-mechanics of chemically active creeping faults: 3. The role of serpentinite in episodic tremor and slip sequences, and transition to chaos. J. Geophys. Res., Solid Earth 119 (6), 4606–4625.

Reber, J.E., Lavier, L.L., Hayman, N.W., 2015. Experimental demonstration of a semi-brittle origin for crustal strain transients. Nat. Geosci. 8 (9), 712.

Rogers, G., Dragert, H., 2003. Episodic tremor and slip on the Cascadia subduction zone: the chatter of silent slip. Science 300 (5627), 1942–1943.

Reynolds, O., 1885. LVII. On the dilatancy of media composed of rigid particles in contact. With experimental illustrations. Philos. Mag. 20 (127), 469–481.

Schwartz, S.Y., Rokosky, J.M., 2007. Slow slip events and seismic tremor at circum-Pacific subduction zones. Rev. Geophys. 45 (3). https://doi.org/10.1029/2006RG000208.

Segall, P., Rubin, A.M., Bradley, A.M., Rice, J.R., 2010. Dilatant strengthening as a mechanism for slow slip events. J. Geophys. Res., Solid Earth 115 (B12).

Shelly, D.R., Beroza, G.C., Ide, S., Nakamula, S., 2006. Low-frequency earthquakes in Shikoku, Japan, and their relationship to episodic tremor and slip. Nature 442 (7099), 188–191.

Shimamoto, T., Noda, H., 2014. A friction to flow constitutive law and its application to a 2-D modeling of earthquakes. J. Geophys. Res., Solid Earth 119 (11), 8089–8106.

Szeliga, W., Melbourne, T., Santillan, M., Miller, M., 2008. GPS constraints on 34 slow slip events within the Cascadia subduction zone, 1997–2005. J. Geophys. Res., Solid Earth 113 (B4), B04404. https://doi.org/10.1029/2007JB004948.

Wakabayashi, J., 2015. Anatomy of a subduction complex: architecture of the Franciscan complex, California, at multiple length and time scales. Int. Geol. Rev. 57 (5–8), 669–746.

Wallace, L.M., Webb, S.C., Ito, Y., Mochizuki, K., Hino, R., Henrys, S., Schwartz, S.Y., Sheehan, A.F., 2016. Slow slip near the trench at the Hikurangi subduction zone, New Zealand. Science 352 (6286), 701–704.

Wang, K., Dragert, H., Kao, H., Roeloffs, E., 2008. Characterizing an "uncharacteristic" ETS event in northern Cascadia. Geophys. Res. Lett. 35 (15).

Wang, K., Hu, Y., He, J., 2012. Deformation cycles of subduction earthquakes in a viscoelastic Earth. Nature 484 (7394), 327–332.

Wilson, D.S., 1993. Confidence intervals for motion and deformation of the Juan de Fuca plate. J. Geophys. Res., Solid Earth 98 (B9), 16053–16071.

Wilson, E.L., 2002. Three Dimensional Static and Dynamic Analysis of Structures. Computers and Structures, Inc., Berkleley, CA.

Xue, L., Li, H.B., Brodsky, E.E., Xu, Z.Q., Kano, Y., Wang, H., Mori, J.J., Si, J.L., Pei, J.L., Zhang, W., Yang, G., 2013. Continuous permeability measurements record healing inside the Wenchuan earthquake fault zone. Science 340 (6140), 1555–1559.

Yasuhara, H., Marone, C., Elsworth, D., 2005. Fault zone restrengthening and frictional healing: the role of pressure solution. J. Geophys. Res., Solid Earth 110 (B6).

Zhang, L., He, C., 2016. Frictional properties of phyllosilicate-rich mylonite and conditions for the brittle–ductile transition. J. Geophys. Res., Solid Earth 121 (4), 3017–3047.